



Research article

Preparation of visible-light active MOFs-Perovskites (ZIF-67/LaFeO₃) nanocatalysts for exceptional CO₂ conversion, organic pollutants and antibiotics degradation

Aftab Khan^{a,1}, Samreen Sadiq^{b,1}, Iltaf Khan^{c,*}, Muhammad Humayun^{d,**}, Guo Jiyuan^{a,***}, Muhammad Usman^e, Abbas Khan^{d,8}, Shoaib Khan^f, Amal Faleh Alanazi^d, Mohamed Bououdina^d

^a Department of Physics, School of Science, Jiangsu University of Science and Technology, Zhenjiang, 212100, China

^b School of Biotechnology, Jiangsu University of Science and Technology, Zhenjiang, 212100, China

^c School of Environmental & Chemical Engineering, Jiangsu University of Science and Technology, Zhenjiang, 212100, China

^d Energy, Water and Environment Lab, College of Humanities and Sciences, Prince Sultan University, Riyadh, 11586, Saudi Arabia

^e Interdisciplinary Research Center for Hydrogen Technologies and Carbon Management (IRC-HTCM), King Fahd University of Petroleum and Minerals, Dhahran, 31261, Saudi Arabia

^f College of Horticulture and Landscape Architecture, Northeast Agricultural University, Harbin, 150030, China

⁸ Department of Chemistry, Abdul Wali Khan University Mardan, 23200, Pakistan

ARTICLE INFO

Keywords:

LaFeO₃ nanosheets

MOFs

CO₂ conversion

Malachite green degradation

Antibiotics decomposition

ABSTRACT

Modern industries rapid expansion has heightened energy needs and accelerated fossil fuel depletion, contributing to global warming. Additionally, organic pollutants present substantial risks to aquatic ecosystems due to their stability, insolubility, and non-biodegradability. Scientists are currently researching high-performance materials to address these issues. LaFeO₃ nanosheets (LFO-NS) were synthesized in this study using a solvothermal method with polyvinylpyrrolidone (PVP) as a soft template. The LFO-NS demonstrate superior performance, large surface area and charge separation than that of LaFeO₃ nanoparticles (LFO-NP). The LFO-NS performance is further upgraded by incorporating ZIF-67. Our results confirmed the ZIF-67/LFO-NS nanocomposite have superior performances than pure LFO-NP and ZIF-67. The integration of ZIF-67 has enhanced the charge separation and promote the surface area of LFO-NS which was confirmed by various characterization techniques including TEM, HRTEM, DRS, EDX, XRD, FS, XPS, FT-IR, BET, PL, and RAMAN. The SZIF-67/LFO-NS sample showed significant activities for CO₂ conversion, malachite green degradation, and antibiotics (cefazolin, oxacillin, and vancomycin) degradation. Furthermore, stability tests have confirmed that our optimal sample very active and stable. Furthermore, based on scavenger experiments and the photocatalytic degradation pathways, it has been established that H⁺ and •O₂⁻ are vital in the decomposition of MG and antibiotics. Our research work will open new gateways to prepare MOFs-Perovskites nanocatalysts for exceptional CO₂ conversion, organic pollutants and antibiotics degradation.

* Corresponding author.

** Corresponding author.

*** Corresponding author.

E-mail addresses: doctortilafkhan@just.edu.cn (I. Khan), mhumayun@psu.edu.sa (M. Humayun), jyguo@just.edu.cn (G. Jiyuan).

¹ The aforementioned authors made an equal contribution to this work.

<https://doi.org/10.1016/j.heliyon.2024.e27378>

Received 20 January 2024; Received in revised form 28 February 2024; Accepted 28 February 2024

Available online 4 March 2024

2405-8440/© 2024 The Authors. Published by Elsevier Ltd. This is an open access article under the CC BY-NC-ND license (<http://creativecommons.org/licenses/by-nc-nd/4.0/>).

1. Introduction

The rapid expansion of modern industries and population has resulted in a higher demand for energy and accelerated the depletion of fossil fuels [1,2]. Excessive CO₂ emissions from fossil fuel combustion and high vehicle usage significantly contribute to global warming which is disrupting the carbon cycle and causing environmental issues [3]. Additionally, Malachite green (MG), a persistent and carcinogenic organic pollutant mainly found in industry manure harms the ecological cycle and humans [4]. Conversely, antibiotics such as cefazolin (CFZ), oxacillin (OXC), and vancomycin (VCM) are commonly introduced into water bodies through hospital waste discharge. Antibiotics have multiple applications and high pharmacokinetics, leading to long-term adverse impacts on aquatic environments due to their long-term stability, insolubleness, and non-biodegradability. Among various approaches, photocatalysis is an eco-friendly method for addressing these environmental issues [5,6].

Recently, researchers have been utilizing semiconductor-based photocatalysis for various applications such as CO₂ conversion, and decomposition of MG and antibiotics. They have been particularly interested in visible-light active and narrow-band gap oxides. In this regard, LaFeO₃ nanoparticles (LFO-NP) possess a narrow band gap, making them an active material under visible light [7]. Nonetheless, LFO-NP shows reduced activity because of its limited surface area, less active sites, and increased charge recombination rate. Therefore, we prepared LaFeO₃ nanosheets (LFO-NS) by using a soft template (PVP) by hydrothermal method [8]. Additionally, LFO-NS exhibit a greater number of visible sites, a high surface area, a significant surface-to-volume ratio, as compared to LFO-NP. Recently, Khan et al. [9] fabricated a g-C₃N₄ and LaFeO₃ nanocomposite for CO₂ reduction and bisphenol A degradation, demonstrating its ecofriendly nature, efficiency, and stability due to enhanced charge separation and electron transportation. In another study, Khan et al. [10] demonstrated the preparation of SnO₂ with LaFeO₃ microspheres, which exhibited significant visible-light photoactivity in degrading dyes. Additionally, Humayun and his research group [11] developed LaFeO₃ and TiO₂ photocatalysts for 2,4-dichlorophenol degradation and conversion of CO₂. The nanocomposite showed significantly higher photocatalytic activities. Moreover, Zhang and colleagues [12] prepared LaFeO₃@Ag using a template and sol-gel method, impregnation methods. The catalysts showed improved photocatalytic performance, stability, and practical applications for antibiotic degradation. The research work indicates that LaFeO₃ is gaining high attention in various research fields. Despite its remarkable photocatalytic activities, the as-prepared LaFeO₃ has limitations such as positive conduction band, high charge recombination, and low activity [13]. To overcome these limitations, various approaches like metal or non-metals doping, modifying its morphology and crystal structure, and coupling other materials with LFO-NS have been employed [14]. In this regard, metal-organic frameworks like ZIF-67 are effective photocatalysts for organic pollutants degradation due to their unique chemical composition, adsorption properties, its narrow band gap (~1.94 eV), high surface area, variable organic ligands, conductivity, porous structure, polymetallic sites, negative CB, excellent stability, cost-effective and high efficiency [15]. Finally, it is demonstrated that the integration of ZIF-67 to LFO-NS offers immense potential in the area of photocatalysis for CO₂ conversion, organic pollutants and antibiotics degradation [16].

Till to date, there appears to be a lack of emphasis on the development of this particular nanocomposite for applications like CO₂ conversion, dyes, and antibiotics decomposition. Ultimately, this research work discusses the successful synthesis and utilization of LFO-NS and ZIF-67 nanocomposites for environmental applications. The most active sample (5ZIF-67/LFO-NS) showed significant activities as compared to pristine LFO-NS. Specifically, there was a 3-fold increase for CO₂ conversion, a 2.6-fold increase for MG decomposition, and a 1.96-fold increase for antibiotics decomposition. Notably, our research has demonstrated that the incorporation of ZIF-67 has significantly boosted the surface area and strengthened the charge separation of LFO-NS through the adjustment of band gap positions. Finally, Our research work will open new gateways to prepare MOFs-Perovskites nanocatalysts for exceptional CO₂ conversion, organic pollutants and antibiotics degradation.

2. Experimental section

2.1. Materials

All the reagents including La(NO₃)₃·6H₂O, Fe(NO₃)₃·9H₂O, polyvinylpyrrolidone (PVP), Co(NO₃)₂·6H₂O, NaOH, ethanol, 2-methylimidazole, methanol, and Malachite green (C₂₃H₂₅ClN₂), cefazolin (C₁₄H₁₄N₈O₄S₃), oxacillin (C₁₉H₁₉N₃O₅S) and vancomycin (C₆₆H₇₅C₁₂N₉O₂₄) employed in this work were purchased from Aladdin Group Co., Ltd. (Beijing, China) and Macklin Biochemical Technology Co., Ltd. (Shanghai, China). All these chemicals and reagents were of analytical grade and used as received without any pretreatment. Deionized water (DI H₂O) was used throughout the experimental work. All the reagents are given in Table S1.

2.2. Preparation of materials

2.2.1. Synthesis of LaFeO₃ nanoparticles (LFO-NP)

LFO-NP are prepared by using a typical method according to which the precursors, Fe(NO₃)₃·9H₂O and La(NO₃)₃·6H₂O, are dissolved in a solvent containing ethanol, and DIH₂O. Followed by ultrasonication, the mixture is placed in a microwave at 85 °C, and subsequently calcined in air at 600 °C for 3 h to yield LFO-NP [17].

2.2.2. Synthesis of LaFeO₃ nanosheets (LFO-NS)

LFO-NS is synthesized via a hydrothermal technique by using PVP as a template. In typical experiment, we mix 0.08 mol of La and Fe precursor in a solution with ethanol and DIH₂O. In next step, PVP is added to the solution and stirred for 45 min. Accordingly, the

solution was transferred into an autoclave for a hydrothermal reaction at 180 °C overnight. Following ethanol water washing process, the product is separated via centrifugation. The product is dried at 80 °C for overnight. After being subjected to calcination at 600 °C for 120 min and finally brown-colored LFO was obtained in the form of nanosheets [18].

2.2.3. Synthesis of MOFs (ZIF-67)

The solvothermal method is employed for preparation of ZIF-67. In standard experiment, the reactants such as $\text{Co}(\text{NO}_3)_2 \cdot 6\text{H}_2\text{O}$ and 2-methylimidazole are dissolved in DMF and methanol and heated in autoclaves at 200 °C. Following ethanol water washing process, the product is separated via centrifugation. The product undergoes drying is dried at 80 °C for overnight. After being subjected to calcination at 400 °C for 120 min, the ZIF-67 is produced [19].

2.2.4. ZIF-67/LaFeO₃ nanosheets based nanocomposite

The ZIF-67/LaFeO₃ nanosheets were prepared by mixing varying mass ratio percentages of ZIF-67 with 1 g of LFO-NS in 200 mL DI water. The solution was stirred for 3 h, then heated to 85 °C and finally followed the calcination process at 600 °C for 3 h [20].

2.2.5. CO₂ photocatalytic activity measurements

The CO₂ conversion activities are performed by dispersing 0.2 g of catalyst in DIH₂O and transferring it to a reactor. The CO₂ is continuously allowed to flow through the reaction system for 30 minutes. After 1 hour of radiation exposure, 0.2 mL of the sample is extracted and then injected into a gas chromatograph equipped with TCD and FID detectors [21].

2.2.6. Organic pollutant degradation activities measurement

MG degradation experiments are conducted in a 100 mL photochemical glass reactor. We added 0.2 g of the catalysts in 80 mL of MG dye solution and stirred it in the dark for 1 h. After this, the solution was stirred under visible light by using a xenon lamp with 420 nm cutoff glass filter. After each 1 h, about 3 mL sample is collected and passed through filters and investigated using the UV spectrophotometer (Shimadzu UV2550). The same experimental procedure is adopted to check the of samples [22].

2.2.7. Antibiotics decomposition activities measurements

The cefazolin (CFZ), oxacillin (OXC), and vancomycin (VCM), decomposition was conducted over pure LFO-NS and most active ZIF-67/LFO-NS samples. [23]. The antibiotic degradation tests were carried out in an open 100 mL photo-chemical glass reactor. In the first step, 0.2 g of as-prepared samples and dispersed in 80 mL solution (10 mg. L⁻¹) of as prepared antibiotic, and continuously stirred for 30 min in dark to attain equilibrium. Consequently, to test the photocatalytic activities the resulting solution was kept under visible-light utilizing a xenon lamp (300 W) with a 420 nm cutoff glass filter. After regular intervals of 1 h, a 3 mL sample were taken with the help of a syringe and filtered. Afterward, a UV spectrophotometer (Shimadzu UV2550) was used to test the filtered samples. Subsequently, we calculated the decomposition activity by equation (1). Adding more, [24] the illustration of experimental design for degradation of pollutants and antibiotics degradation is shown in Fig. S1.

$$D\% = (A_0 - A_t) / A_0 \times 100 \quad (1)$$

The decomposition rates (D%) of CFZ, OXC, and VCM, as well as their initial concentrations A_0 and A_t , and absorbance at t intervals, may be influenced by factors such as pH, concentration, and the amount of decomposing material [25].

2.3. Characterization of materials

The as prepared materials are characterized by employing diverse characterization techniques, such as X-ray diffraction (XRD) to identify their crystal structure on a diffractometer at 30 kV and 20 mA current. We confirmed the samples' elemental composition through XPS while the binding energy of the samples was verified using a carbon signal (284.55 eV). Morphology of samples is investigated by Transmission electron microscopy (TEM) (Talos-(F200x)-FTEM (FEI, Netherland) and Scanning electron microscopy (SEM) (Hitachi Regulus810) at 200 kV. The UV-visible DRS spectra with BaSO₄ as a reference was checked by Shimadzu UV-2550 spectrophotometer. An advanced instrument, the MIKE ASAP2460, 2020 was used to analyze Brunauer-Emmett-Teller (BET) and adsorption-desorption isotherms. [26].

3. Results and discussions

In this research study, we used a hydrothermal and solvothermal technique to synthesize LFO-NS and ZIF-67 and ZIF-67/LFO-NS based. Our research findings demonstrate that ZIF-67/LFO-NS is a highly potent photocatalyst for reducing CO₂, and degrading MG, and various antibiotics. Moreover, our results showed that ZIF-67/LFO-NS composite exhibited a better performance than the pristine LFO-NS and ZIF-67. In addition, the fabrication of ZIF-67 increases the surface area of LFO-NS and improves charge separation. The detailed investigations, novelty and the finding are given below

3.1. Exploring LFO-NS potential over LFO-NP

In this research work, we designed a high-performance, effective, and large surface area LFO-NS by using polyvinylpyrrolidone

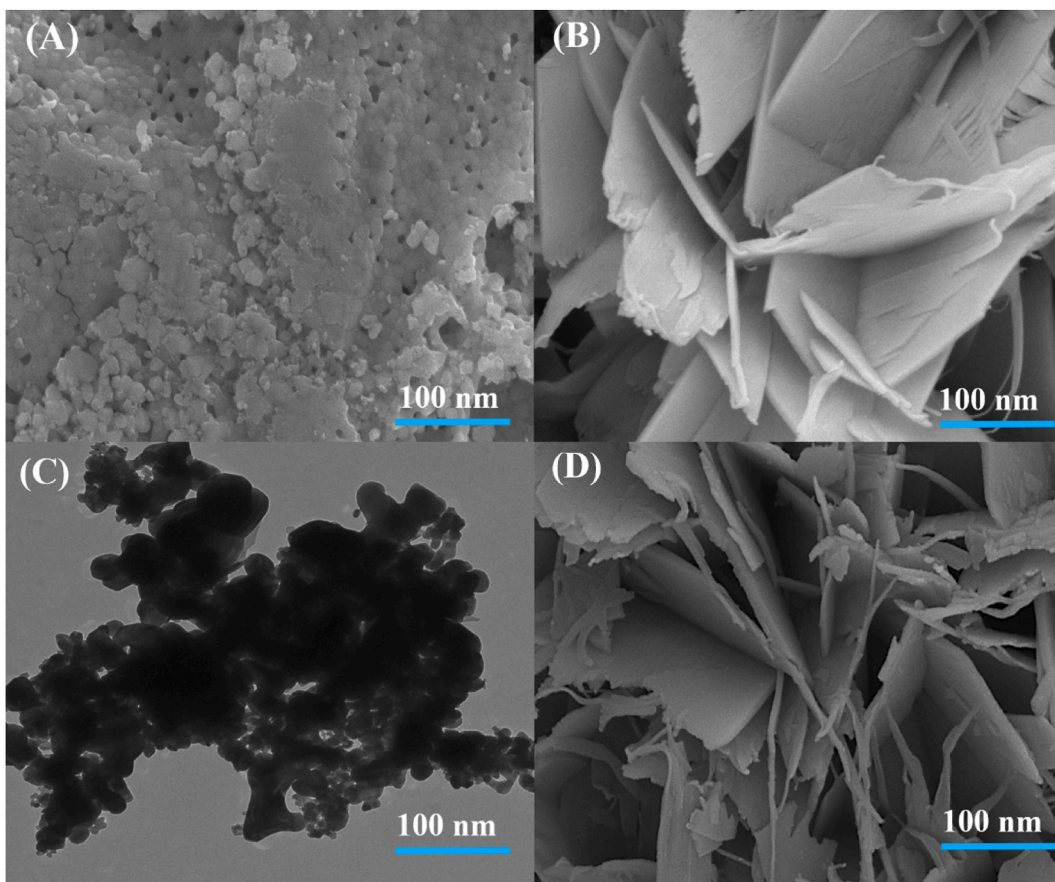


Fig. 1. SEM images (A, B), TEM images (C, D) of LFO-NP and LFO-NS.

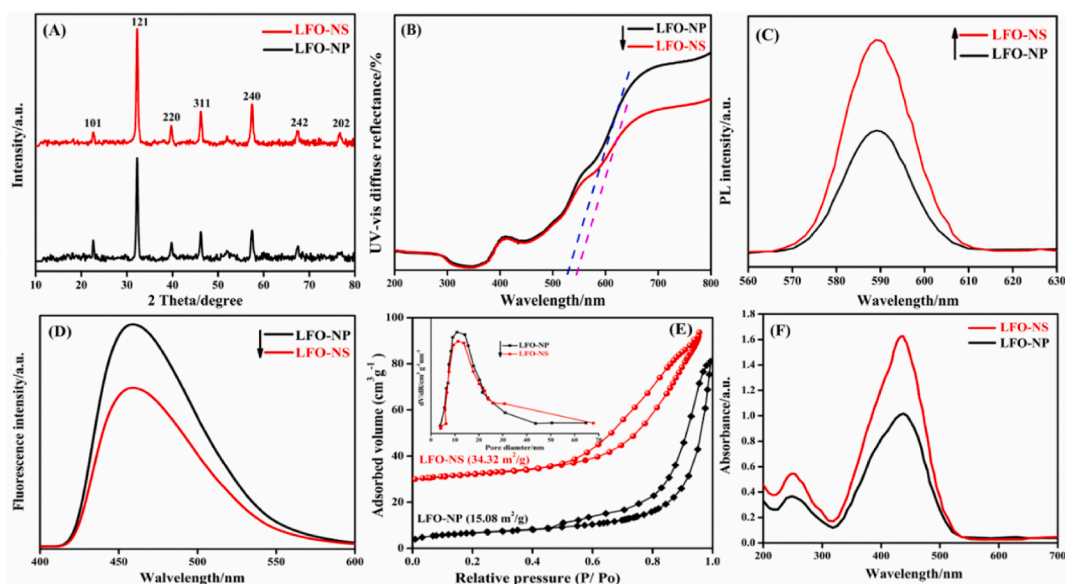


Fig. 2. XRD peaks (A), DRS spectrum (B), PL (C), FS spectra (D), BET graph with pore diameter as inset (E), and UV absorbance spectra (F) of LFO-NP and LFO-NS.

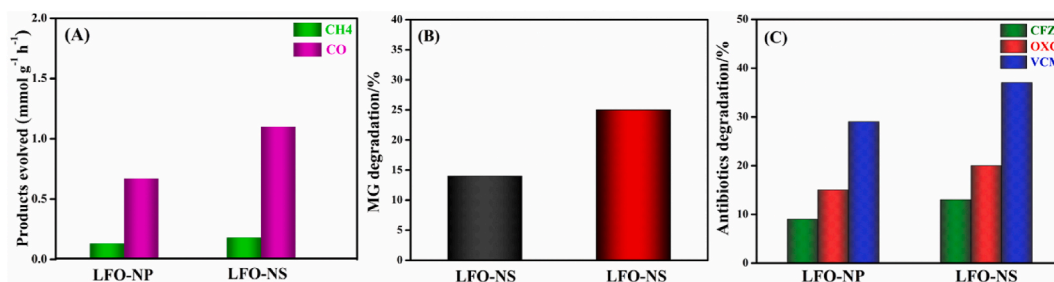


Fig. 3. CO₂ conversion (A), MG degradation (B), antibiotics decomposition (C) of LFO-NP and LFO-NS.

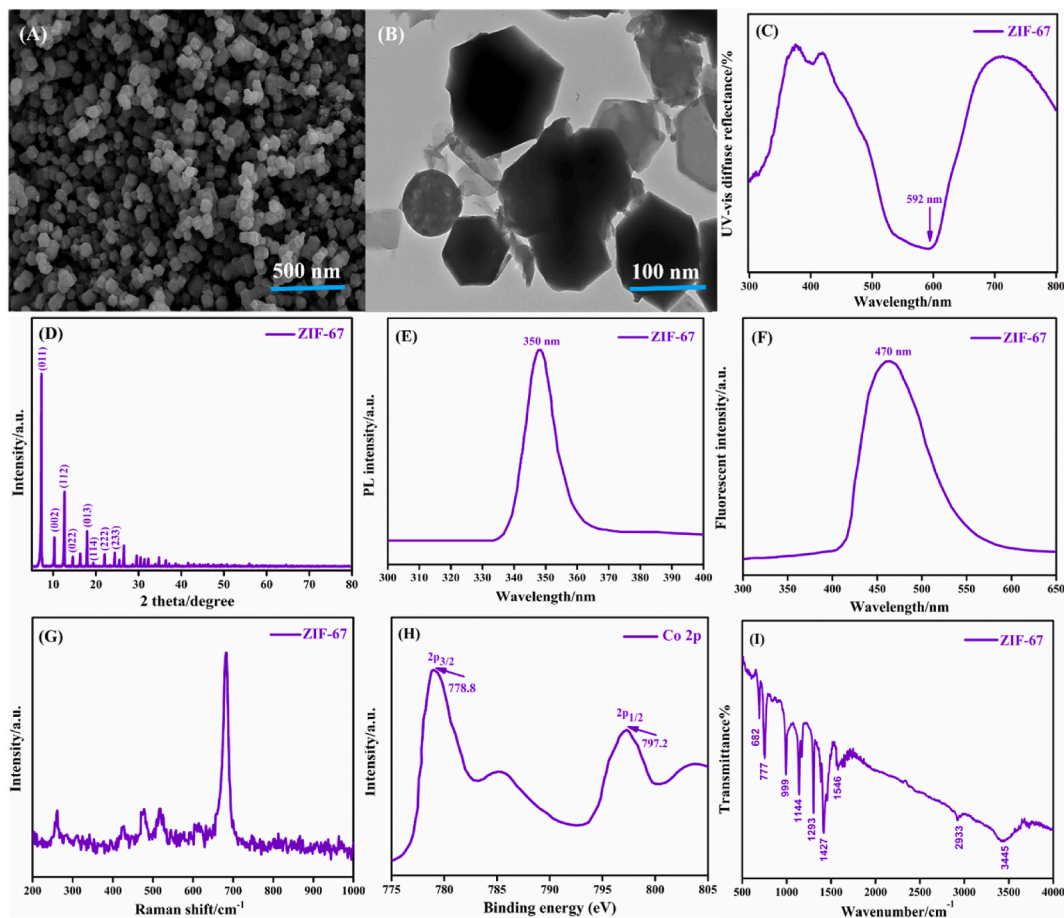


Fig. 4. TEM (A, B), DRS (C), XRD (D), PL (E), FS (F), Raman (G), XPS (H) and FT-IR (I) of ZIF-67.

(PVP) as soft template. The results confirmed that LFO-NS is more efficient than LFO-NP [27]. To verify the superior photocatalytic performance of LFO-NS over LFO-NP catalyst, various physicochemical characterization techniques were used. The SEM results of LFO-NP and LFO-NS in Fig. 1A and B while TEM images of LFO-NP and LFO-NS in Fig. 1C and D, shows the presence of nanoparticles aggregation, and rough surface [28]. On the other hand, SEM and TEM images of LFO-NS sheets without aggregation, well exfoliated, high surface area leading to active sites for reduction of CO₂, organic pollutants and antibiotics degradation [29].

Interestingly, the LFO-NS have layered nanosheets, broad light absorption range, high surface area, precise band gap positioning, and improved stability, than LFO-NP [30]. Fig. 2A reveals diffraction peaks at 2 theta values of 26.5°, 33.9°, 37.9°, 51.8°, 54.8°, 61.9°, and 78.8° which correspond to (101), (121), (220), (311), (240), (242), and (202) planes that exhibit the high crystallinity of LFO-NS as compared to LFO-NP due to relatively high intensity of peaks. In addition, the band gap of the as-prepared samples was investigated via DRS [31]. Fig. 2B illustrates that LFO-NS with an absorption peak at 620 nm which suggests that LFO-NS band gap present in the visible light region so will have excellent catalytic efficiency [32]. In addition, PL spectra indicate the charge separation. So, Fig. 2C

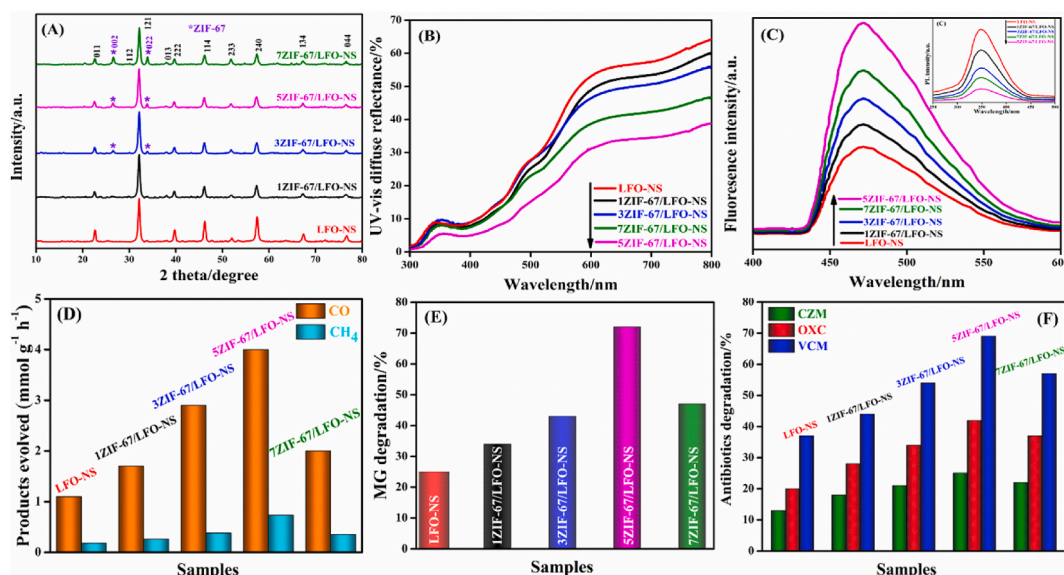


Fig. 5. XRD (A), DRS spectra (B), FS spectra as inset PL spectra (C), CO₂ conversion (D), MG degradation (E), and antibiotics degradation (F) of ZIF-67/LFO-NS.

shows LFO-NS have high light excitation at 590 nm, indicating superior activities of LFO-NS over LFO-NP [33]. Furthermore, Fig. 2D indicates an enhanced fluorescence intensity peak at 470 nm, signifying improved charge separation of LFO-NS than LFO-NP [34]. Furthermore, the BET measurements illustrated in Fig. 2E confirmed the surface area of LFO-NS (34.32 m²/g) that exceeds to LFO-NP (15.08 m²/g) while in Fig. 2F it can be observed that the LFO-NS have high UV absorbance than LFO-NP. In brief, based on our findings, LFO-NS has a high surface area, high charge separation and higher performance than LFO-NP. So, LFO-NS can be used for multifunctional applications [35].

Fig. 3A–B and C show exceptional results for conversion of CO₂, MG and antibiotics decomposition respectively. Remarkably, it is obvious that as compared to LFO-NP, the LFO-NS showed 2-fold, 2.2-folds and 1.4-fold higher activities for CO₂, MG, and antibiotics degradation respectively. Hence, it has been verified that the photocatalytic results of LFO-NS surpass those of LFO-NP. The higher photocatalytic activity are due to large surface area, more active sites, and efficient light absorption. Hence, it is confirmed that LFO-NS is more efficient and stable than LFO-NP.

3.2. Exploring the importance of MOFs (ZIF-67)

In our current research work, we have successfully synthesized ZIF-67. Fig. 4A and B demonstrate the rhombic dodecahedral shape of ZIF-67, typically varying in size from 100 to 500 nm. In addition, the DRS shown in Fig. 4C highlights a clear peak at 592 nm in the UV region, suggesting the excellent light absorption capacity of ZIF-67 in UV region [36]. Moreover, the XRD patterns in Fig. 4D demonstrate the crystal structure and validate the synthesis of the ZIF-67. The XRD is utilized for identifying the phase nature and crystal structure based on diffraction peaks at specific 2 theta values of (011), (002), (112), (022), (013), (222), (114), (233), (134), and (044) [37]. In addition, Fig. 4E shows a peak at 350 nm indicating a strong distinction between charges and recombination of electron-hole pairs in the visible spectrum [38]. Moreover, fluorescence intensity shown in Fig. 4F, displays a peak at 470 nm which shows the more generation of •OH [39]. Furthermore, in Fig. 4G the raman spectroscopy was used to analyze ZIF-67 deeply. The peak at 680 cm⁻¹ confirming the successful formation of ZIF67 [40]. Additionally, the elemental nature and chemical composition of ZIF-67 are identified using XPS, as illustrated in Fig. 4H. The binding energy of Co elements is associated with the Co 2p peaks, suggesting a 2-oxidized state of Co (II) or Co (III) in ZIF-67 [41]. Adding more, Fig. 4I demonstrated an FT-IR analysis which was conducted to investigate the chemical nature. The peaks at 682, 777, 999, 1144, 1293, 1546, 1427, 2930, and 3445 cm⁻¹ consistent with previous studies: 6 [42]. Based on FT-IR a correlation between Co and nitrogen atoms of the 2-methylimidazole ligand is found. This correlation led to distinct bands associated with Co–N stretched vibrations, C=N stretching, and C–H sp³ aromatic ring [43].

3.3. Constructing MOFs-Perovskites nanocomposite (ZIF-67 and LFO-NS)

3.3.1. Structural characterizations

Although, LFO-NS has better efficiency as compared to LFO-NP as discussed in the above section, but still as-synthesized LFO-NS has some issues regarding smaller surface area, charge separation, and positive CB [44]. On the other hand, ZIF-67 has numerous superior features like high porosity, suitable band gaps, polymetallic sites, and negative CB [45]. With the intention to improve charge separation, surface area, and adjust CB of LFO-NS, we fabricated the different mass percentages of YZIF-67 (where Y = 1%, 3%, 5%,

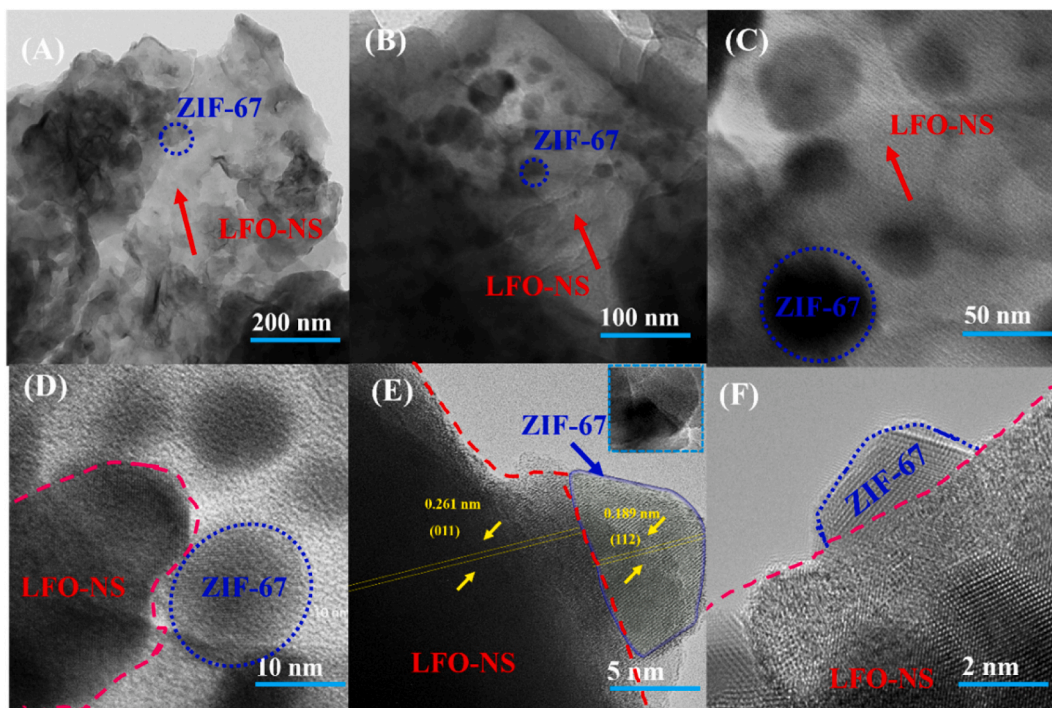


Fig. 6. TEM images (A, B, C), HRTEM images (D, E, F) of 5ZIF-67/LFO-NS nanocomposite.

and 7%) with LFO-NS through wet chemical and grinding methods. Fruitfully, the positive CB of the LFO-NS was fine-tuned to an optimal position, improving charge separation by regulating the excited photoelectrons. In order to examine the physical properties and structural nature of the composite, the crystallinity and structure of the YZIF-67/LFO-NS (with $Y = 1\%$, 3% , 5% , and 7%) were investigated by XRD. According to the XRD patterns, the pristine LFO-NS has six distinct peaks at 9.7° , 22.6° , 32.3° , 39.6° , 44.1° and 63.4° corresponding to 011, 121, 013, 222, 114, 233, 240, 134 and 044 crystal planes [46]. The dominant presence of ZIF-67 in 5ZIF-67/LFO-NS is confirmed at 7.6° (002) and 10.6° (022) [47] which can be clearly seen in Fig. 5A. Additionally, Fig. 5B shows DRS spectrum of fabricated composites, indicating that pristine LFO-NS emits light at 340 nm, validating the band gap at 2.0 eV [48]. Meanwhile, the band gap relocated to the visible area upon integrating with different mass percentage ratios of ZIF-67 to LFO-NS. The band gap position of the 5ZIF-67/ZIF-8 nanocomposite was revealed to be around 620 nm, indicating that the composite is more visible-light active than pristine LFO-NS [49]. Fig. 5C illustrates the fluorescence peak at 470 nm generated by the combination of LFO-NS and ZIF-67, despite a limited charge separation. The amount of $\bullet\text{OH}$ rises when ZIF-67 was added. Furthermore, the PL spectra of ZIF-67 given in Fig. 5C (inset) indicate the PL spectra of LFO-NS decreased after coupling with ZIF-67 confirming enhanced charge separation with the optimal sample (5ZIF-67/LFO-NS) having the highest response [50]. In addition, Fig. 5D demonstrated the photocatalytic activities of LFO-NS for CO_2 conversion. The pristine LFO-NS showed poor activity about $0.18 \text{ mmol g}^{-1} \text{ h}^{-1}$ for CH_4 and $1.1 \text{ mmol g}^{-1} \text{ h}^{-1}$ for CO production. However, significant improvement in photocatalytic activity was observed upon coupling with various percentages of ZIF-67 [51]. The optimal sample 5ZIF-67/LFO-NS showed 2.5-folds and 3-folds enhancements for CH_4 and CO production respectively but excessive ZIF-67 increase led to decreased CO production due covering surface of LFO-NS. So, our findings demonstrated that the optimal sample (5ZIF-67/LFO-NS) exhibited efficient visible-light photoactivities [52]. Moreover, Fig. 5E illustrates that ZIF-67 significantly improves the photocatalytic performance of LFO-NS, the optimal sample exhibiting a 2.6 times higher degradation activity for MG degradation as compared to pristine LFO-NS [53]. Furthermore, Fig. 5F demonstrates that integrating various amounts of ZIF-67 significantly enhances the photocatalytic performance of LFO-NS, the optimal sample showing 1.94-fold greater antibiotic degradation activity.

The integration of ZIF-67 significantly increases the surface area of LFO-NS as demonstrated by the N_2 adsorption-desorption isotherm graph in (Fig. S2A). Remarkably, the surface area of 5ZIF-67/LFO-NS was improved by $314 \text{ m}^2/\text{g}$ i.e., a 3-fold increase compared to pure LFO-NS [54]. However, the pore size of LFO-NS decreased after ZIF-67 integration as shown in (Fig. S2B) resulting in an enlarged surface area for CO_2 conversion, MG, and antibiotics degradation leading to intermediate production and inorganic minerals [55].

Our study confirmed that the 5ZIF-67/LFO-NS composite showed superior efficiency and was the most active sample among all composites. TEM and HRTEM analysis was performed on an efficient sample, 5ZIF-67/LFO-NS, which showed the successful loading of ZIF-67 onto LFO-NS as demonstrated in Fig. 6A–B and C. The HRTEM of the best sample (5ZIF-67/LFO-NS) reveals fringe lines as depicted in Fig. 6D–E, and Fig. 6F. Notably, Fig. 6E shows two clear fringes with specific d-spacing values for LFO-NS and ZIF-67, corresponding to the (011) and (112) lattice planes [56,57].

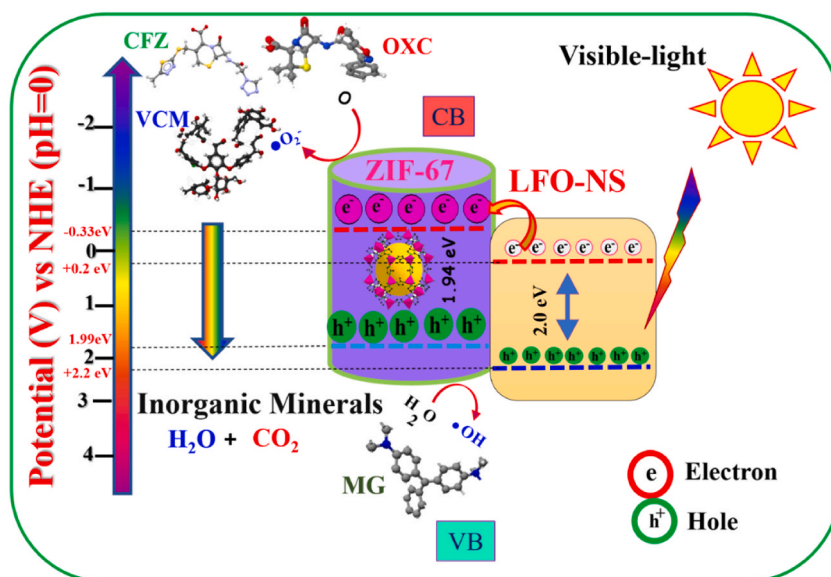


Fig. 7. Graphical representation for Z-scheme bandgaps and charge separation of LFO-NS and ZIF-67.

Furthermore, we have selected the sample (5ZIF-67/LFO-NS) for TEM (EDX) analysis and elemental mapping in order to examine its elemental characteristics and chemical composition of most active samples. The overall overlay (Fig. S3A), color overlay (Fig. S3B), O (Fig. S3C), Co (Fig. S3D), La (Fig. S3E), and Fe (Fig. S3F) were present in the sample confirming that ZIF-67 was effectively incorporated into LFO-NS. The percentages of O, Co, La and Fe in 5ZIF-67/LFO-NS were also shown in Fig. S4.

3.4. Antibiotics decomposition activities measurements

It is confirmed that coupling of ZIF-67 to LFO-NS effectively increased the overall activity. Notably, 5ZIF-67/LFO-NS is the most active and effective sample. However, as the amount of ZIF-67 increased, the degradation activity decreased, as it blocked the active sites and pores of LFO-NS, making it unable to adsorb more materials on the surface [58]. Most importantly, the 5ZIF-67/LFO-NS indicated good degradation activities for CFZ (2-folds), OXC (2.1-folds), and VCM (1.86-folds) more proficiently than pristine LFO-NS and their degradation activities and time dependent graphs are depicted in Fig. S5 (A, B), Fig. S6 (A, B), and Fig. S7 (A, B) respectively.

4. Mechanism insights

Herein in this research work, we fruitfully synthesized ZIF-67/LFO-NS based composite via PVP. The PVP TGA as shown in Fig. S8, confirms that this template is very stable. The LFO-NP have shown low photocatalytic activity due to its low charge separation, positive CB, particles accumulation, and low surface area [59]. Therefore, we have successfully synthesized LFO-NS to improve photocatalytic activities. The visible activity of LFO-NS is suboptimal because of its higher positive CB, lower surface area, and reduced charge separation. Therefore, ZIF-67 was coupled with LFO-NS owing to the substantial surface area, negative CB, high charge separation, and more reactive sites [25]. Remarkably, integrating ZIF-67 with LFO-NS greatly expands the surface area, and charge carrier mobility, and promotes productive charge separation. Exploring the charge transfer mechanism, energy band gaps, and energy levels of ZIF-67/LFO-NS are illustrated in Fig. 7 demonstrating that the LFO-NS has a narrow band gap (2.0 eV). Conversely, ZIF-67, are visible light active, provides dual functionality by enhancing surface adsorption through photoelectron modulation and increasing charge separation by accepting high-energy electrons. More importantly, with a band gap of 1.94 eV, it exhibits activity in the visible region [60]. The coupling of ZIF-67 provides a platform for charge transportation via photoelectrons modulation, leading to improved activities and enhance charge separation [61]. Additionally, the ZIF-67 aCB platform is suitable to receive excited photoelectrons from LFO-NS and absorb high-energy electrons, thereby activating surface for CO₂ conversion, MG and antibiotics degradation [62].

On mechanism point of view, the catalytic CO₂ conversion, organic pollutants and antibiotics degradation over our designed materials are mainly involved with the production and separation of electron (e⁻)/hole (h⁺) pairs. The components in a catalyst play a crucial role in the oxidation and reduction of pollutants. The h⁺ oxidizes pollutants directly or reacts with water, generating •OH radicals. On the catalyst surface, oxygen is reduced to O₂•⁻, transforming organic pollutants into inorganic minerals and converting CO₂ into valuable products.

Furthermore, energy band gaps, photo-excitation nature of energy carriers, activities improvement are illustrated in Fig. 7 and Fig. S9A. The coupling ZIF-67 promotes charge transfer, which in turn increases charge separation and activity rates. To verify the improvement and transmission of charges, Photo current action (PCA) spectra were performed utilizing sunlight at a range of

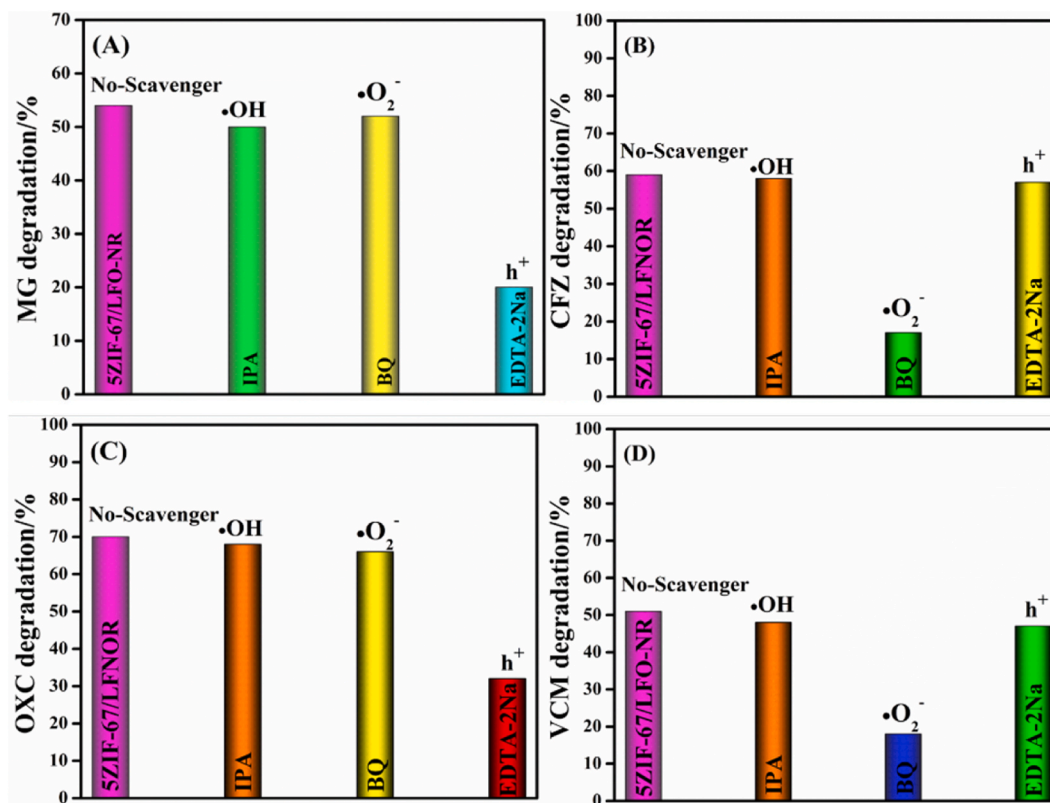


Fig. 8. Scavenger test for MG (A), CFZ (B), OXC (C), and VCM (D) degradation 5ZIF-67/LFO-NS.

modulations (630–810 nm). The, Fig. S9B shows that 5ZIF-67/LFO-NS increases PCA density at 650 nm, aligning with LFO-NS. This increased current density allows photoexcited species like electrons and holes to be accessible for longer periods.

Furthermore, the elemental composition of the best sample (5ZIF-67/LFO-NS) was analyzed by XPS as shown in Fig. S10. The spectrum indicates the effective loading of ZIF-67 onto LFO-NS, with distinct peaks for Co, oxygen, nitrogen, and carbon at 800 eV, 530 eV, 570 eV, 400 eV and 280 eV respectively. Adding more, Fig. S11 shows the separate spectra of each element. So, the XPS spectra of La (Fig. S11A), Fe (Fig. S11B), O (Fig. S11C), and Co (Fig. S11D) confirmed that our samples were successfully prepared.

The FT-IR spectrum of LFO-NS and 5ZIF-67/LFO-NS related to imidazole ring stretching, and C=N bonds as shown in Fig. S12 indicating the fruitful integration of ZIF-67 onto LFO-NS [63]. Moreover, Raman spectroscopy was employed to further confirm the effective synthesis of 5ZIF-67/LFO-NS as given Fig. S13. The 5ZIF-67/LFO-NS nanocomposite exhibits a distinct peak at 680 nm corresponding to ZIF-67.

In order to understand more about the mechanism of charge transfer in 5ZIF-67/LFO-NS different experiments were conducted including Z'Ohm, PEC (IV) and PEC (light). In short, the Fig. S14A confirm the superior performance of 5ZIF-67/LFO-NS in enhancing photogenerated charges under visible-light irradiation than pure LFO-NS [64]. In addition, Fig. S14B further supported the measurement of photoelectrochemical I–V curves. The sample demonstrates a limited photocurrent density reaction under visible-light exposure. However, the performance is greatly improved with the introduction of ZIF-67, leading to a noticeable photocurrent response in the 5ZIF-67/LFO-NS sample. Moreover, Fig. S14C shows that the pure LFO-NS has a low PEC response after the light is turned off, but it greatly enhances when combined with ZIF-67 under light [65]. Notably, 5ZIF-67/LFO-NS showed a superior response to light, leading to improved photocatalytic performance for CO₂ conversion and antibiotic breakdown via improving charge separation and minimizing electron and hole recombination rates [66].

Our resulting ZIF-67/LFO-NS nanocomposite demonstrates exceptional porosity, high , and excellent potential for adsorption, rendering it very efficient for MG and antibiotic degradation [67]. In this research work we also investigated the primary species that initiates degradation reactions for MG, CFZ, OXC, and VCM by using radical scavenging methods. BQ, IPA, and EDTA-2Na were used to scavenge •OH, h⁺, and •O₂⁻ respectively Fig. 8A shows the degradation of MG by using 5ZIF-67/LFO-NS with different active species. The findings propose that the activation of the process is attributed to the presence of BQ related h⁺ ions, whereas •O₂⁻ and •OH do not have a major effect whereas as shown in Fig. 8B the presence of IPA containing •O₂⁻ species greatly influenced the efficacy of degrading CFZ using 5ZIF-67/LFO-NS. This suggests that •O₂⁻ rather than h⁺ or •OH, is the main active species responsible for stimulating CFZ breakdown activities. Furthermore, Fig. 8C indicates that the degradation of OXC by 5ZIF-67/LFO-NS, BQ related h⁺ is responsible for activating the reaction, whereas •O₂⁻ and •OH has no effect. Additionally, the degradation of VCM using 5ZIF-67/LFO-NS and various active species shows that the response is stimulated by negatively charged (•O₂⁻) whereas h⁺ or •OH have no effect as shown in Fig. 8D.

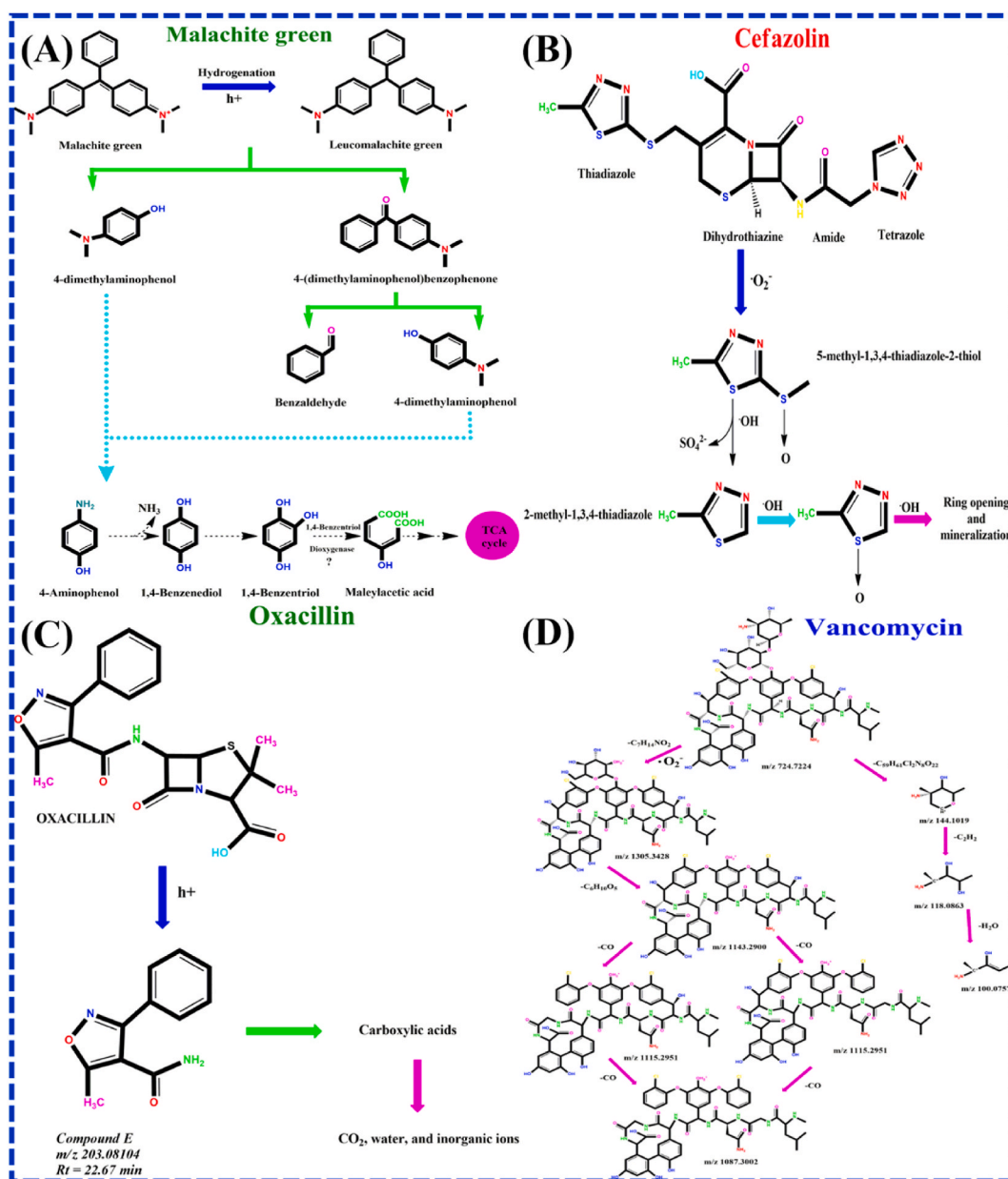


Fig. 9. Malachite green (A), Cefazolin (B), Oxacillin (C), and Vancomycin (VCM) degradation pathway over 5ZIF-67/LFO-NS. (For interpretation of the references to color in this figure legend, the reader is referred to the Web version of this article.)

In this research study we also investigate the formation of inorganic minerals from organic pollutants including MG, CFZ, OXC, and VCM by using 5ZIF-67/LFO-NS and explore the formation of intermediate molecules. The results revealed that the 5ZIF-67/LFO-NS significantly degraded the MG, CFZ, OXC, and VCM, with a degradation rate of 72%, 25%, 42%, and 69%, respectively. In short, our designed current nanocomposite is proving to be very effective environmental remediation. The degradation mechanism of organic pollutants i.e malachite green as shown in Fig. 9A, cefazolin in Fig. 9B, oxacillin in Fig. 9C, and vancomycin in Fig. 9D over 5ZIF-67/LFO-NS is also proposed [68–71].

Moreover, in order to investigate the influence of hydrothermal processing, high-temperature calcination and chemical stability of 5ZIF-67/LFO-NS. The model pollutant (MG) was recollected, washed, centrifuged, dried and reused upto 5-times at various concentrations (50, 75, and 100 m/L); (Fig. S15A). This highlights that the activities decrease when we cross the optimum concentration of organic pollutants i.e 75 m/L [72]. In addition, stability tests given in Fig. S15B further confirm that our samples are stable. Finally, the structural stability of the original and recovered ZIF-67/LFO-NS samples were confirmed by XRD patterns (Fig. S16A), samples weight stability (Fig. S16B), TGA (Fig. S16C), activities tests (Fig. S16D). These results confirmed that before and after various catalytic

reactions our samples are highly stable.

5. Conclusion

In this research work, we used hydrothermal and solvothermal approaches to synthesize LFO-NS using PVP as a soft template. The efficiency of resulting LFO-NS was further upgraded by coupling with different percentages of MOFs i.e ZIF-67. Our study shows that the incorporation of ZIF-67 into LFO-NS significantly enhanced its functionality by adjusting the positions of band gaps, increasing surface area, and enhancing charge separation through photo-electron modulation. Electro-analytical and physicochemical characterization methods confirmed that compared to pristine LFO-NS, the most active sample 5ZIF-67/LFO-NS showed a three-fold improvement in CO₂ conversion activities. Furthermore, 5ZIF-67/LFO-NS exhibited degradation activities of 72% for MG, 25% for CFZ, 42% for OXC, and 69% for VCM. Moreover, the degradation pathways of the organic pollutants are also deeply investigated. Adding more, the stability and recyclability of the most active sample (5ZIF-67/LFO-NS) are evaluated. Finally, our research will new ground plan to synthesize MOFs-Perovskites based nanomaterials that are active under visible light and efficient for CO₂ conversion, organic pollutants degradation, and environmental remediation.

Ethical approval

There are no human subjects in this article and informed consent is not applicable.

Consent to publish

The results/data/figures in this manuscript have not been published elsewhere, nor are they under consideration by another publisher.

Availability of data and materials

Data is available on request from the authors.

CRediT authorship contribution statement

Aftab Khan: Writing – review & editing, Writing – original draft, Conceptualization. **Samreen Sadiq:** Writing – review & editing, Writing – original draft, Validation, Software, Methodology, Conceptualization. **Iltaf Khan:** Supervision, Resources, Funding acquisition. **Muhammad Humayun:** Validation, Methodology, Funding acquisition. **Guo Jiyuan:** Supervision, Conceptualization. **Muhammad Usman:** Validation, Software, Data curation. **Abbas Khan:** Visualization, Software, Resources, Formal analysis. **Shoaib Khan:** Software, Methodology, Data curation. **Amal Faleh Alanazi:** Validation, Software, Resources. **Mohamed Bououdina:** Software, Data curation.

Declaration of competing interest

The authors declare that they have no known competing financial interests or personal relationships that could have appeared to influence the work reported in this paper.

Acknowledgments and Fundings

The authors are grateful and would like to thank the National Natural Science Foundation of China (Grant No. 22150410332) and Jiangsu University of Science and Technology (Grant No. 1112932205) for financial support. The author would like to acknowledge the support provided by the Saudi Aramco Chair Program (ORCP2390), Authors are grateful and would like to thank Prince Sultan University Riyadh for paying the Article Processing Charges (APC).

Appendix A. Supplementary data

Supplementary data to this article can be found online at <https://doi.org/10.1016/j.heliyon.2024.e27378>.

References

- [1] M. Adeel, et al., Synthesis and characterization of Co–ZnO and evaluation of its photocatalytic activity for photodegradation of Methyl Orange, *ACS Omega* 6 (2) (2021) 1426–1435.
- [2] I. Khan, et al., Bio-capped and green synthesis of ZnO/g-C₃N₄ nanocomposites and its improved antibiotic and photocatalytic activities: an exceptional approach towards environmental remediation, *Chin. J. Chem. Eng.* 56 (2023) 215–224.

- [3] K. Kang, et al., Recent advances in the synthesis and application of magnetic biochar for wastewater treatment, *Bioresour. Technol.* 390 (2023) 129786.
- [4] M. Saeed, et al., Synthesis of p-n NiO-ZnO heterojunction for photodegradation of crystal violet dye, *Alex. Eng. J.* 65 (2023) 561–574.
- [5] K. Bhise, et al., Combination of vancomycin and cefazolin lipid nanoparticles for overcoming antibiotic resistance of MRSA, *Materials* 11 (7) (2018).
- [6] A.L. Giraldo, et al., Degradation of the antibiotic oxacillin in water by anodic oxidation with Ti/IrO₂ anodes: evaluation of degradation routes, organic by-products and effects of water matrix components, *Chem. Eng. J.* 279 (2015) 103–114.
- [7] I. Khan, et al., Green synthesis of SrO bridged LaFeO₃/g-C₃N₄ nanocomposites for CO₂ conversion and bisphenol A degradation with new insights into mechanism, *Environ. Res.* 207 (2022) 112650.
- [8] Y. Zhu, et al., Construction of a hollow BiOI/TiO₂/ZIF-8 heterojunction: enhanced photocatalytic performance for norfloxacin degradation and mechanistic insight, *J. Alloys Compd.* 914 (2022) 165326.
- [9] I. Khan, et al., Synthesis of phosphate-bridged g-C₃N₄/LaFeO₃ nanosheets Z-scheme nanocomposites as efficient visible photocatalysts for CO₂ reduction and malachite green degradation, *Appl. Catal. Gen.* 629 (2022) 118418.
- [10] I. Khan, et al., Synthesis of SnO₂/yolk-shell LaFeO₃ nanocomposites as efficient visible-light photocatalysts for 2,4-dichlorophenol degradation, *Mater. Res. Bull.* 127 (2020) 110857.
- [11] M. Humayun, et al., Exceptional visible-light activities of TiO₂-coupled N-doped porous perovskite LaFeO₃ for 2,4-dichlorophenol decomposition and CO₂ conversion, *Environmental Science & Technology* 50 (24) (2016) 13600–13610.
- [12] H. Zhang, et al., Synthesis and formaldehyde sensing performance of LaFeO₃ hollow nanospheres, *Phys. E Low-dimens. Syst. Nanostruct.* 63 (2014) 21–26.
- [13] I. Khan, et al., Enhanced visible-light photoactivities of porous LaFeO₃ by synchronously doping Ni²⁺ and coupling TS-1 for CO₂ reduction and 2,4,6-trinitrophenol degradation, *Catal. Sci. Technol.* 11 (20) (2021) 6793–6803.
- [14] R. Gao, et al., Oxygen defects-engineered LaFeO₃-x nanosheets as efficient electrocatalysts for lithium-oxygen battery, *J. Catal.* 384 (2020) 199–207.
- [15] S. Khan, et al., Eco-friendly graphitic carbon nitride nanomaterials for the development of innovative biomaterials: preparation, properties, opportunities, current trends, and future outlook, *J. Saudi Chem. Soc.* 27 (6) (2023) 101753.
- [16] S. Nazari, et al., Visible-light-driven photocatalytic activity of WO₃/ZIF-67 S-scheme heterojunction for upgrading degradation of oxytetracycline, *J. Environ. Chem. Eng.* 11 (5) (2023) 110393.
- [17] V. Berbenni, et al., Synthesis and characterization of LaFeO₃ powders prepared by a mixed mechanical/thermal processing route, *Journal of Thermal Analysis and Calorimetry* 133 (1) (2018) 413–419.
- [18] B.M. Pirzada, et al., Synthesis of LaFeO₃/Ag₂CO₃ nanocomposites for photocatalytic degradation of rhodamine B and p-chlorophenol under natural sunlight, *ACS Omega* 4 (2) (2019) 2618–2629.
- [19] C. Wang, et al., Facile synthesis of metal-organic framework ZIF-67 via a multi-inlet vortex mixer using various solvents: MeOH, EtOH, H₂O, and baijiu, *Ind. Eng. Chem. Res.* 61 (23) (2022) 7952–7961.
- [20] J. Liu, et al., ZIF-67 derived LaCoO₃/Co₃O₄ nanoparticles/g-C₃N₄ P-N junction with enhanced photodynamic antibacterial performance, *Appl. Surf. Sci.* 643 (2024) 158720.
- [21] A. Hayat, et al., Molecules conjugated electron donor-acceptor hybrid polymeric carbon nitride as a photocatalyst for CO₂ reduction, *Molecules* (2019) 24.
- [22] M. Saeed, et al., Synthesis of CoO-ZnO photocatalyst for enhanced visible-light assisted photodegradation of methylene blue, *New J. Chem.* 46 (2022).
- [23] S. Zaman, et al., Synthesis of mediator free hollow BiFeO₃ spheres/porous g-C₃N₄ Z-scheme photocatalysts for CO₂ conversion and Alizarin Red S degradation, *Mater. Sci. Semicond. Process.* 162 (2023) 107534.
- [24] J. Wu, et al., Single-atom Pt anchored thiophene ring doped carbon nitride nanosheets for enhanced visible-light photocatalytic H₂ evolution and ciprofloxacin degradation, *Int. J. Hydrogen Energy* (2023).
- [25] K. Qi, et al., Photocatalytic H₂ generation via CoP quantum-dot-modified g-C₃N₄ synthesized by electroless plating, *Chin. J. Catal.* 41 (1) (2020) 114–121.
- [26] W. Yaseen, et al., Facile synthesis of CoMoO₄/CoMoB/boron-doped carbon nanocomposite as a highly durable bifunctional electrocatalyst for overall water splitting, *Int. J. Hydrogen Energy* 51 (2024) 565–577.
- [27] I. Khan, et al., Efficient Visible-Light Activities of TiO₂ decorated and Cr³⁺-incorporated-porous SmFeO₃ for CO₂ conversion and 4-chlorophenol degradation, *Surface. Interfac.* 34 (2022) 102358.
- [28] T. Hai, et al., Designing g-C₃N₄/ZnCo₂O₄ nanocomposite as a promising photocatalyst for photodegradation of MB under visible-light excitation: response surface methodology (RSM) optimization and modeling, *J. Phys. Chem. Solid.* 185 (2024) 111747.
- [29] H. Asghar, et al., Synthesis of g-C₃N₄/SmFeO₃ nanosheets Z-scheme based nanocomposites as efficient visible light photocatalysts for CO₂ reduction and Congo red degradation, *J. Mater. Res.* 38 (11) (2023) 2986–2997.
- [30] M. Khan, et al., Experimental and DFT Study of GO-Decorated CaO Quantum Dots for Catalytic Dye Degradation and Bactericidal Potential, 2023, p. 11.
- [31] D.M. Ikram, et al., Fabrication of La-doped MoS₂ nanosheets with tuned bandgap for dye degradation and antimicrobial activities, experimental and computational investigations, *Adv. Mater. Interfac.* 10 (2023).
- [32] N. Sharma, et al., Fabrication of LaFeO₃ and rGO-LaFeO₃ microspheres based gas sensors for detection of NO₂ and CO, *RSC Adv.* 10 (3) (2020) 1297–1308.
- [33] J. Song, et al., Photocatalytic degradation of tetracycline hydrochloride with g-C₃N₄/Ag/AgBr composites, *Front. Chem.* 10 (2022) 1069816.
- [34] M. Saeed, et al., Synthesis of p-n NiO-ZnO heterojunction for photodegradation of crystal violet dye, *Alex. Eng. J.* 65 (2022).
- [35] W. Aimee, et al., MOF-derived porous carbon-supported bimetallic Fischer-Tropsch synthesis catalysts, *Ind. Eng. Chem. Res.* 61 (2022) 3941–3951.
- [36] W. Yaseen, et al., Facile solvothermal synthesis of boron-doped carbon-based comoo4/comob nanocomposite as a bifunctional electrocatalyst for overall water splitting, *SSRN Electron. J.* (2022).
- [37] A.G. Dymerska, et al., In situ insight into the low-temperature promotion of ZIF-67 in electrocatalytic oxygen evolution reaction, *Mater. Des.* 226 (2023) 111637.
- [38] X.-M. Zhou, et al., Development of a rapid visual detection technology for BmNPV based on CRISPR/Cas13a system, *J. Invertebr. Pathol.* 203 (2024) 108072.
- [39] N.T. Tran, L.G. Trung, M.K. Nguyen, The degradation of organic dye contaminants in wastewater and solution from highly visible light responsive ZIF-67 monodisperse photocatalyst, *J. Solid State Chem.* 300 (2021) 122287.
- [40] B. Weckhuysen, M. Filez, Z. Öztürk, Decoding nucleation and growth of Zeolitic imidazolate framework Thin-films with atomic force microscopy and vibrational spectroscopy, *Chemistry (Weinheim an der Bergstrasse, Germany)* 23 (2017).
- [41] X.-D. Du, et al., Extensive and selective adsorption of ZIF-67 towards organic dyes: performance and mechanism, *J. Colloid Interface Sci.* 506 (2017) 437–441.
- [42] M. Afkhami-Ardekani, et al., Solvent-free mechanochemical preparation of metal-organic framework ZIF-67 impregnated by Pt nanoparticles for water purification, *Catalysts* 13 (2022) 9.
- [43] S. Sadiq, et al., Synthesis of metal-organic framework-based ZIF-8@ZIF-67 nanocomposites for antibiotic decomposition and antibacterial activities, *ACS Omega* 8 (51) (2023) 49244–49258.
- [44] Z.-k. Chen, et al., Hsp90 could promote BmNPV proliferation by interacting with Actin-4 and enhance its expression, *Dev. Comp. Immunol.* 142 (2023) 104667.
- [45] I. Khan, et al., Graphitic carbon nitride composites with gold and ZIF-67 nanoparticles as visible-light-promoted catalysts for CO₂ conversion and bisphenol A degradation, *ACS Appl. Nano Mater.* 5 (9) (2022) 13404–13416.
- [46] N. Sharma, et al., The Comparative Study of One Step and Two Step rGO-LaFeO₃ Composite, vol. 2265, 2020 030681.
- [47] M. Usman, et al., Propene adsorption-desorption behaviors on H-SAPO-34 zeolite catalysts at different temperatures, *Catalysts* 9 (2019), <https://doi.org/10.3390/catal9110919>.
- [48] G. Iervolino, et al., LaFeO₃ modified with Ni for hydrogen evolution via photocatalytic glucose reforming in liquid phase, *Catalysts* 11 (2021) 1558.
- [49] M. Usman, et al., Poly aromatic hydrocarbon (naphthalene) conversion into value added chemical (tetralin): activity and stability of MoP/AC catalyst, *J. Environ. Chem. Eng.* 6 (4) (2018) 4525–4530.
- [50] S. Acharya, D. Kandi, K. Parida, CdS QD decorated LaFeO₃ nanosheets for photocatalytic application under visible light irradiation, *ChemistrySelect* 5 (2020) 6153–6161.

- [51] S. Ullah, et al., First-principles calculations to investigate optical properties of topological semimetal MX compounds (M = Ti, Zr, Hf and X = S, Se, Te), *Mater. Today Commun.* 35 (2023) 106001.
- [52] M. Usman, M.H. Suliman, Silver-Doped zeolitic imidazolate framework (Ag@ZIF-8): an efficient electrocatalyst for CO₂ conversion to syngas 13 (5) (2023) 867.
- [53] S. Jabeen, et al., Photocatalytic degradation of malachite green dye via an inner transition metal oxide-based nanostructure fabricated through a hydrothermal route 14 (1) (2023) 5.
- [54] A. Ehsani, et al., Ternary nanocomposite of TiO₂-ZnO/MCM-41: synthesis and electrochemical performance in supercapacitors, *J. Energy Storage* 50 (2022) 104633.
- [55] S. Sadiq, et al., Recent updates on multifunctional nanomaterials as antipathogens in humans and livestock: classification, application, mode of action, and challenges, *Molecules* 28 (2023), <https://doi.org/10.3390/molecules28227674>.
- [56] N. Torad, et al., Electric double-layer capacitors based on highly graphitized nanoporous carbons derived from ZIF-67, *Chem. Eur J.* 20 (2014).
- [57] M. Saeed, et al., Synthesis of a CoO–ZnO photocatalyst for enhanced visible-light assisted photodegradation of methylene blue, *New J. Chem.* 46 (5) (2022) 2224–2231.
- [58] E. Asgari, et al., Enhancement the BuP photo-catalytic degradability by UVC/ZnO through adding exogenous oxidant: mechanism, kinetic, energy consumption, *J. Environ. Chem. Eng.* 8 (1) (2020) 103576.
- [59] H. Godini, et al., Energy consumption and photochemical degradation of Imipenem/Cilastatin antibiotic by process of UVC/Fe²⁺/H₂O₂ through response surface methodology, *Optik* 182 (2019) 1194–1203.
- [60] A. Hayat, et al., Conjugated electron donor–acceptor hybrid polymeric carbon nitride as a photocatalyst for CO₂ reduction 24 (9) (2019) 1779.
- [61] S. Sadiq, et al., A critical review on metal-organic frameworks (MOFs) based nanomaterials for biomedical applications: designing, recent trends, challenges, and prospects, *Heliyon* 10 (3) (2024) e25521.
- [62] S. Chen, et al., Improved photoactivities for CO₂ conversion and phenol degradation of α -Fe₂O₃ nanoparticles by co-coupling nano-sized BiPO₄ and CuO to modulate electrons, *J. Alloys Compd.* (2019) 800.
- [63] Z. Huang, et al., Stable core–shell ZIF-8@ZIF-67 MOFs photocatalyst for highly efficient degradation of organic pollutant and hydrogen evolution, *J. Mater. Res.* 36 (3) (2021) 602–614.
- [64] I. Khan, et al., Efficient CO₂ conversion and organic pollutants degradation over Sm³⁺ doped and rutile TiO₂ nanorods decorated-GdFeO₃ nanorods, *Int. J. Hydrogen Energy* 48 (84) (2023) 32756–32770.
- [65] J. Wu, et al., Single-atom Pt anchored thiophene ring doped carbon nitride nanosheets for enhanced visible-light photocatalytic H₂ evolution and ciprofloxacin degradation, *Int. J. Hydrogen Energy* 51 (2024) 1138–1150.
- [66] M. Yaseen, et al., Efficient structure tuning over the defective modulated zirconium metal organic framework with active coordinate surface for photocatalyst CO₂ reduction, *J. Colloid Interface Sci.* 653 (2024) 370–379.
- [67] H. Tang, et al., ZIF-8/ZIF-67 Derived Carbon for Efficient Removal of Antibiotics in Aqueous Solution, 2019, p. 490.
- [68] H.-F. Xiang, et al., Efficient biodegradation of malachite green by an artificial enzyme designed in myoglobin, *RSC Adv.* 11 (26) (2021) 16090–16095.
- [69] Y. Fan, et al., Degradation mechanisms of ofloxacin and cefazolin using peroxymonosulfate activated by reduced graphene oxide-CoFe₂O₄ composites, *Chem. Eng. J.* 383 (2020) 123056.
- [70] E. Takács, et al., Elimination of oxacillin, its toxicity and antibacterial activity by using ionizing radiation, *Chemosphere* 286 (2022) 131467.
- [71] M. Cao, et al., Studies on the metabolism and degradation of vancomycin in simulated in vitro and aquatic environment by UHPLC-Triple-TOF-MS/MS, *Sci. Rep.* 8 (1) (2018) 15471.
- [72] B. Ai, M. Luo, I. Khan, Effective malachite green degradation over the noble metal-doped and MOF-coupled CsSnBr₃ nanocomposite catalyst, *Processes* 11 (2023), <https://doi.org/10.3390/pr11051398>.